Membrane oscillations driven by Arp2/3 constrict the intercellular bridge during neural stem cell divisions

Bryce LaFoya and Kenneth E. Prehoda[1]

Institute of Molecular Biology
Department of Chemistry and Biochemistry
1229 University of Oregon
Eugene, OR 97403

[1]Corresponding author: prehoda@uoregon.edu

Summary

1   After the first furrowing step of animal cell division, the nascent sibling cells remain connected

2   by a thin intercellular bridge (ICB). In isolated cells nascent siblings migrate away from each

3   other to generate tension and constrict the ICB, but less is known about how cells complete

4   cytokinesis when constrained within tissues. We examined the ICBs formed by *Drosophila*

5   larval brain neural stem cell (NSC) asymmetric divisions and find that they rely on constriction

6   focused at the central midbody region rather than the flanking arms of isolated cell ICBs.

7   Super-resolution, full volume imaging revealed unexpected oscillatory waves in plasma

8   membrane sheets surrounding the ICB pore during its formation and constriction. We find that

9   these membrane dynamics are driven by Arp2/3-dependent branched actin networks.

10   Inhibition of Arp2/3 complex activity blocks membrane oscillations and prevents ICB formation

11   and constriction. Our results identify a previously unrecognized role for localized membrane

12   oscillations in ICB function when cells cannot generate tension through migration.

Introduction

15   Cell division in animal cells proceeds through three sequential membrane constriction steps[1]

16   (Fig. 1A). First, a broad actomyosin ring rapidly constricts the plasma membrane between the

17   segregated chromosomes until the connecting pore reaches a diameter of ~1.5 μm. The

18   intercellular bridge (ICB) – a membranous tube containing the compacted central spindle –

19   connects the nascent siblings after the initial furrowing step[2]. The ICB then undergoes a slower

20   constriction phase, narrowing to ~200 nm in diameter, before the final step of abscission

21   severs the membrane connection between the daughter cells[3–5]. While the molecular

22   mechanisms driving initial furrowing and final abscission are relatively well understood, the

23   intermediate phase of ICB constriction remains poorly characterized. Most insights come from

24   studies of cultured cells, where the ICB forms a long, thin tube as the nascent siblings actively

25   migrate apart[2,6]. This ICB consists of a central midbody flanked by constricting arms (in an

26   alternate nomenclature ICB and midbody are synonymous and the central structure is the stem

27   body)[2,7–10]. When the arms narrow to ~200 nm, the midbody-recruited ESCRT-III resolves the

28   membrane during abscission[3,11–13]. Here we address how ICB constriction occurs in cells that

29   are part of a tissue, where mechanical constraints may preclude the nascent sibling separation

30   that occurs in cultured cells.

31   The ICB forms when the central spindle becomes compacted in the cytokinetic pore through

32   the action of the first furrowing step (Fig. 1A). The region of the central spindle with overlapping

33   microtubules coated with proteins such as PRC1 and centralspindlin form the midbody[14,15]

34   while the adjacent flanking arms are the sites of constriction[5,16]. Flanking arm constriction gives

35   rise to the characteristic ICB shape with two thin tubes surrounding a thicker midbody[3,11–13,17].

36   In cultured cells, membrane tension generated by migration of the nascent sibling cells

37   contributes to the structure of the ICB and is also thought to drive arm constriction. While

38   tension appears to be necessary for the formation and function of the ICB, abscission requires

39   low tension. These different requirements suggests that cells must carefully regulate

40   membrane tension to complete the final steps of cytokinesis. However, cells within tissues face

41   mechanical constraints that could prevent tension generation by migration-based mechanisms.

42   To understand ICB constriction in such an environment, we examined the asymmetrically

43   dividing neural stem cells (NSCs) of the *Drosophila* larval brain (Fig. 1B).

44   NSCs divide rapidly, generating a larger self-renewed stem cell and a smaller neural

45   precursor[18–20]. The initial furrow formation in NSCs is well-characterized, with both spindle- and

46   polarity-dependent signals positioning the actomyosin ring[21–26]. As the initial furrow completes

47   the first phase of NSC furrowing, cortical actomyosin flows are directed away from the

48   equatorial region[27,28]. However, the subsequent ICB phase is poorly understood, including its

49   structure and requirements for constriction. Here we investigate the mechanisms controlling

50   this critical intermediate phase of cytokinesis in tissue-resident stem cells.

51   **Results**

52   **The NSC intercellular bridge is a constricting midbody that lacks conventional flanking**

53   **arms**

54   Larval brain NSCs divide in a highly constrained environment, surrounded on one side by a

55   cortex glial cell and the other by progeny from previous asymmetric divisions (Fig. 1B). We

56   sought to understand how the NSC ICB functions in this environment given the extended

57   structure of canonical ICBs. ICB arms are membranous tubes filled with microtubules that lack

58   midbody proteins such as centralspindlin and PRC1 (Fascetto in *Drosophila*)[14,15,29]. We

59   examined the structure of the NSC ICB using super resolution microscopy while monitoring the

60   plasma membrane with PLCδ-PH along with microtubules or the centralspindlin protein MKLP1

61   (Pavarotti in *Drosophila*). The ICB forms when the cytokinetic pore reaches a diameter of

62   approximately 1.5 µm when microtubules, Pavarotti (Pav), and other proteins become

63   compacted within the pore. We observed several important differences between NSC and

64   canonical ICBs (Fig. 1C-H; Video 1). First, the NSC ICB appeared to consist solely of the

65   midbody, as no part of the membrane tube lacked Pav (Fig. 1H; Video 1). Second, the NSC

66   ICB constricted at the midbody (Fig. 1H; Video 1). Finally, while formation of the canonical ICB

67   is correlated with migration of nascent sibling cell bodies away from one another, the NSC

68   nascent sibling membranes move in the opposite direction, becoming compressed against one

69   another (Fig. 1E). Together, these data suggest that asymmetrically dividing neuroblasts form

70   an intercellular bridge that lacks the conventional tripartite organization, instead consisting

71   solely of a midbody.

72   **Sheets of plasma membrane oscillate near the cytokinetic pore during ICB formation and**

73   **constriction**

74   The plasma membrane is remodeled near the cytokinetic pore late in cytokinesis[30,31]. We

75   examined the membrane remodeling in detail to determine if it is related to ICB formation or

76   constriction. We imaged the full volume of the cytokinetic pore and surrounding membrane

77   along with microtubules, revealing a highly dynamic process where sheets of plasma

78   membrane formed simultaneously with midbody formation (Fig. 2A; Video 2). The sheets are

79   formed in an oscillatory pattern such that they appear as waves emanating from the pore that

80   extended into the cytoplasm (Fig. 2A,B; Video 2). The waves appeared predominantly on the

81   side of the pore of the larger, NSC nascent sibling, although we cannot exclude the possibility

82   that some membrane remodeling occurs on the other side. The oscillations of plasma

83   membrane sheets continued through the ICB constriction process. Thus, we conclude that ICB

84   formation and constriction is correlated with dramatic remodeling of the plasma membrane

85   around the pore, where large sheets of oscillating membrane form around the pore for the

86   duration of ICB thinning.

87   **Plasma membrane oscillations near the pore are driven by F-actin**

88   We sought to understand the cellular processes that drive membrane remodeling near the ICB

89   pore. We imaged F-actin along with the membrane to determine if actin polymerization might

90   be correlated with the oscillating membrane sheets as F-actin has been reported to be

91   localized to protrusions that form late in NSC cytokinesis[31]. When imaging F-actin, we

92   observed dense actin networks surrounding the membrane sheets, and these networks were

93   highly correlated with sheet oscillations (Fig. 3A,B; Video 3). While a small amount of cortical

94   actin was present before membrane sheet formation, a large burst of actin appeared when the

95   deformations of the membrane around the pore began. Clouds of actin that surrounded the

96   membrane sheets continued during the ICB thinning process. While strong F-actin signal

97   surrounded the membrane oscillations near the pore, the signal within the pore was much

98   more limited, especially early in the process when the pore was at its largest.

99   We sought to identify the cytoskeletal proteins that regulate or cooperate with sheet-

100   associated actin. The formin F-actin nucleator Diaphanous (Dia), was strongly enriched on the

101   wall of the ICB (Fig. 3C; Video 3), but we did not detect it in the surrounding membrane sheets.

102   We observed Myosin II broadly distributed on the equatorial cortex during the initial furrowing

103   stage (Fig 3D; Video 3). Immediately before ICB formation, Myosin II dissipated from the furrow

104   as previously described[28], before becoming strongly enriched on the ICB wall. We did not

105   detect any significant Myosin II localization with the membrane sheets that surround the ICB

106   pore. We conclude that the F-actin associated with the membrane sheets surrounding the ICB

107   pore is not nucleated by Dia and is not part of an actomyosin contractile network.

108   **Arp2/3 actin filament nucleation is required for NSC ICB thinning**

109   We also examined the localization of a nucleator of branched actin networks, the Arp2/3

110   complex. The Arp-3 subunit localized specifically to sites of plasma membrane remodeling

111   surrounding the pore and was recruited shortly before the burst of actin that coincides with

112   membrane sheet formation (Fig. 4A; Video 4). The Arp2/3 activator SCAR (aka WAVE complex)

113   localizes to the NSC furrow[31] and we observed localization to the membrane sheets that form

114   around the ICB (Fig. 4B; Video 4). To examine the function of the Arp2/3 complex in membrane

115   remodeling and ICB function, we acutely inhibited its activity using the chemical inhibitor CK-

116   666. Arp2/3 inhibition before ICB formation completely abrogated membrane sheet formation

117   and caused stalling of the furrow at a diameter of approximately 1.5 µm (Fig. 4C,D; Video 4).

118   We also inhibited Arp2/3 after membrane sheet oscillations had initiated and the midbody had

119   formed. In these cells, membrane sheet dynamics and ICB constriction abruptly stopped (Fig.

120   4E; Video 4). We conclude that Arp2/3 is required for the membrane oscillations near the ICB,

121   and for ICB formation and constriction.

122   **Discussion**

123   In this study, we addressed a fundamental gap in our understanding of cytokinesis - how cells

124   complete division when constrained within tissues, where they may not be able to generate

125   tension across the ICB through migration like isolated cells do. We make the key discovery that

126   Drosophila larval brain NSCs utilize a distinct ICB structure during cytokinesis, characterized

127   by constriction focused at the central midbody rather than flanking arms. We also reveal

128 previously unrecognized oscillatory membrane dynamics surrounding the ICB that depend on

129 Arp2/3-mediated branched actin networks.

130 We propose that the unique structure of the NSC ICB, lacking the conventional tripartite

131 organization with flanking arms, may represent an adaptation for cells dividing within tissues.

132 While isolated cells can generate tension across their ICB through migration, tissue-resident

133 cells face mechanical constraints that may prevent such movement. Indeed, we observe that

134 NSC daughter cells become compressed against each other rather than separating when the

135 ICB forms (Fig. 1E). The focused constriction at the midbody, rather than along extended arms,

136 could allow these cells to complete cytokinesis without requiring active migration of the

137 nascent sibling cells away from one another.

138 The dramatic membrane remodeling we observe around the ICB, with oscillating membrane

139 sheets driven by Arp2/3-dependent actin networks, may serve to generate localized forces that

140 facilitate bridge constriction in the absence of migration-based tension. This is reminiscent of

141 how Arp2/3 remodels membranes during processes like endocytosis, where branched actin

142 networks provide force for membrane deformation[32,33]. The correlation between membrane

143 oscillations and ICB constriction, along with the complete block of constriction when Arp2/3 is

144 inhibited, suggests these dynamics play an essential role. We propose that the membrane

145 waves could generate mechanical forces that aid in bridge closure or help regulate membrane

146 tension across the ICB in a way that promotes sufficient constriction to allow abscission to

147 take place.

148 **Resource Availability**

149 **Lead Contact**

150 Contact the Lead Contact, Kenneth Prehoda (prehoda@uoregon.edu), for further information or
151 to request resources and reagents.

152 **Materials Availability**

153 No new reagents were generated in this study.

154 **Data and Code Availability**

155 Raw data available from the corresponding author on request.

Experimental Model and Subject Details

Fly Strains

A Worniu-GAL4 driver line was used to drive tissue specific expression of UAS controlled transgenes in neural stem cells (NSCs). Membrane dynamics were imaged using various membrane markers. UAS-PLCδ-PH-GFP and UAS-PLCδ-PH-mCherry express the pleckstrin homology domain of human PLCδ tagged with GFP or mCherry, and binds to the plasma membrane lipid phosphoinositide PI(4,5)P_2. UAS-GRP1-PH-GFP expresses the pleckstrin homology domain of GRP1, and binds to the plasma membrane lipid phosphoinositide PI(3,4,5)P_3[34]. UAS-Farnesyl-GFP expresses the C-terminal region of human K-Ras tagged with GFP which becomes farnesylated and membrane-anchored in cells. F-Actin was visualized using UAS-GMA-GFP, which expresses a GFP tagged actin binding domain of Moesin, and UAS-Lifeact-mRuby. Microtubules were imaged using UAS-Zeus-mCherry. Anillin was imaged using UAS-Anillin-GFP. Arp2/3 was imaged using UAS-Arp3-GFP. Centralspindlin dynamics were imaged using GFP tagged Pavarotti (Pav) protein under control of ubiquitin regulatory sequences. The formin, Diaphanous, was imaged using UAS-Diaphanous-GFP. The SCAR/WAVE complex was imaged using Sra1/Cyfip endogenously tagged with eGFP using CRISPR/Cas9[35]. Myosin II was imaged using GFP tagged Spaghetti squash, the regulatory light chain of non-muscle type II Myosin, expressed from its endogenous promoter[36].

Method Details

Live Imaging

To obtain brain explants, third instar *Drosophila* larvae were dissected in Schneider's Insect Media (SIM) to isolate the central nervous system. Brain explants were mounted on sterile poly-D-lysine coated 35mm glass bottom dish (ibidi Cat#81156) containing modified minimal hemolymph-like solution (HL3.1). Brain explants were imaged using a Nikon Eclipse Ti-2 Yokogawa CSU-W1 SoRa spinning disk microscope equipped dual Photometrics Prime BSI sCMOS cameras using a 60x H_2O objective. 488 nm light was used to illuminate GFP tagged proteins and 561 nm light was used to illuminate mCherry and mRuby tagged proteins. Super resolution imaging was achieved by using SoRa (super resolution through optical photon reassignment) optics [37]. NSCs were identified by their large size, location in the central nervous system, and the use of NSC specific tissue driver lines. Time lapse imaging of cleavage furrow and intercellular bridge dynamics was achieved by refocusing the imaging plane on the medial plane of the cleavage furrow and intercellular bridge, along the apical-basal axis just before capturing each frame. Pharmacological inhibition of the Arp2/3 complex was performed using 2 mM CK666 solubilized in DMSO.

Image Processing and Analysis

Imaging data was processed using ImageJ (FIJI package). For some movies, the bleach correction tool was used to correct for photobleaching. To reduce noise in Arp3-GFP and SCAR-GFP images, Gaussian blur was applied. When image deconvolution was applied, deconvolution was performed using Nikon Elements standard 2D deconvolution mode and noted in the figure/video legend. For cytokinetic pore size measurements, medial sections were used to measure the width of the cytokinetic pore.

197   Quantifying the effects of Arp2/3 inhibition of membrane dynamics during the late stages of NSC
198   division: Closure of the cytokinetic pore was measured for CK666-treated NSCs and compared
199   to untreated NSCs. For quantifying the dynamics of the cytokinetic pore size, medial sections
200   (along the apical-basal axis) were used to measure the width of the cytokinetic pore.

201   **Key Resources Table**

REAGENT or RESOURCE	SOURCE	IDENTIFIER
Experimental Model: Fly Strains		
Anillin-GFP	Bloomington *Drosophila* Stock Center (BDSC)	BDSC Cat#51348 RRID: BDSC 51348
Arp3-GFP (Arp2/3 complex marker)	Bloomington *Drosophila* Stock Center (BDSC)	BDSC Cat#39722 RRID: BDSC 39722
Diaphanous-GFP	Bloomington *Drosophila* Stock Center (BDSC)	BDSC Cat#56751 RRID: BDSC 56751
Myosin II-GFP (GFP tagged Spaghetti squash, the regulatory light chain of non-muscle type II Myosin)	Roger Karess Lab[36]	
Pavarotti (Pav)-GFP (centralspindlin marker)	Bloomington *Drosophila* Stock Center (BDSC)	BDSC Cat#81651 RRID: BDSC 81651
SCAR-GFP (Sra1 tagged with GFP and marks the SCAR/WAVE complex)	Sally Horne-Badovinac Lab[35]	
UAS-Farnesyl-GFP (Farnesylated GFP that marks the plasma membrane)	Bloomington *Drosophila* Stock Center (BDSC)	BDSC Cat#80052 RRID: BDSC 80052
UAS-GMA-GFP (F-actin marker)	Bloomington *Drosophila* Stock Center (BDSC)	BDSC Cat#31776 RRID: BDSC 31776
UAS-GRP1-PH-GFP membrane marker that binds PI(3,4,5)P_3 lipids	Patrik Verstreken Lab[34]	
UAS-Lifeact-mRuby (F-actin marker)	Bloomington *Drosophila* Stock Center (BDSC)	BDSC Cat#35545 RRID: BDSC 35545
UAS-PLCδ-PH-GFP membrane marker that binds PI(4,5)P_2 lipids	Bloomington *Drosophila* Stock Center (BDSC)	BDSC Cat#39693 RRID: BDSC 39693
UAS-PLCδ-PH-mCherry (membrane marker that binds PI(4,5)P_2 lipids)	Bloomington *Drosophila* Stock Center (BDSC)	BDSC Cat#51658 RRID: BDSC 51658
UAS-Zeus-mCherry (microtubule marker)	Chris Q. Doe Lab	
Worniu-GAL4 (NSC driver line)	Chris Q. Doe Lab	
Pharmacological Inhibitors		
CK666	Cayman Chemical	Cat#29038

202

Video Legends

Video 1: Larval brain neural stem cell intercellular bridges are midbodies without flanking arms

Part 1: Membrane and microtubule dynamics during the late stages of NSC division. Super resolution videos of an NSC expressing Zeus-mCherry "Microtubules" and the membrane marker Farnesyl-GFP "membrane". The top row depicts a medial section where the entire cell is visible. The bottom row is a zoomed-in view of the cleavage furrow. Time relative to start of imaging is indicated.

Part 2: Phosphoinositide localization during the late stages of NSC division. Super resolution videos of an NSC expressing the membrane markers UAS-GRP1-GFP "PI(3,4,5)P$_3$" and UAS-PLCδ-PH-mCherry "PI(4,5)P$_2$". The top row a medial section where the entire cell is visible. The bottom row is a zoomed-in view of the cleavage furrow. Time relative to start of imaging is indicated.

Part 3: Anillin and membrane dynamics during the late stages of NSC division. Super resolution videos of an NSC expressing Anillin-GFP "Anillin" and the membrane marker UAS-PLCδ-PH-mCherry "membrane". The top row depicts a medial section where the entire cell is visible. The bottom row is a zoomed-in view of the cleavage furrow. Time relative to start of imaging is indicated.

Part 4: Pavrotti and membrane dynamics during the late stages of NSC division. Super resolution videos of an NSC expressing Pavarotti-GFP "Pavarotti" and the membrane marker UAS-PLCδ-PH-mCherry "membrane". The top row depicts a medial section where the entire cell is visible. The bottom row is a zoomed-in view of the cleavage furrow. Time relative to start of imaging is indicated.

Video 2: Plasma membrane oscillations near the cytokinetic pore during intercellular bridge formation and constriction

Part 1: 3-dimensional view of membrane and microtubule dynamics during the late stages of NSC division. Super resolution videos of an NSC expressing Zeus-mCherry "Microtubules" and the membrane marker Farnesyl-GFP "membrane". Maximum intensity projections of multiple optical sections spanning the cleavage furrow are shown. Time relative to anaphase onset is indicated.

Part 2: Top-down view Anillin and membrane dynamics during the late stages of NSC division. Super resolution videos of an NSC expressing Anillin-GFP "Anillin" and the membrane marker UAS-PLCδ-PH-mCherry "membrane". A single optical section is shown. Time relative to start of cytokinetic pore constriction is indicated.

Video 3: F-actin localizes to plasma membrane waves near the cytokinetic pore

Part 1: Actin and membrane dynamics during the late stages of NSC division. Super resolution videos of an NSC expressing Lifeact-mRuby "Actin" and the membrane marker UAS-PLCδ-PH-GFP "membrane". The top row depicts a medial section where the entire cell is visible. The bottom row is a zoomed-in view of the cleavage furrow. Time relative to anaphase onset is indicated. Image deconvolution was applied.

Part 2: Top-down view Actin and membrane dynamics during the late stages of NSC division. Super resolution videos of an NSC expressing GMA-GFP "Actin" and the membrane marker UAS-PLCδ-PH-mCherry "membrane". A single optical section is shown. Time relative to start of cytokinetic pore constriction is indicated.

Part 3: Myosin II and membrane dynamics during the late stages of NSC division. Super resolution videos of an NSC expressing Myosin II-GFP "Myosin II" and the membrane marker UAS-PLCδ-PH-mCherry "membrane". The top row depicts maximum intensity projections of an entire hemisphere of the dividing NSC. The bottom row is a medial section. The left column shows a view of the whole cell, and the columns to the right are zoomed-in views of the cleavage furrow. Time relative to anaphase onset is indicated.

Part 4: Diaphanous and membrane dynamics during the late stages of NSC division. Super resolution videos of an NSC expressing Diaphanous-GFP "Diaphanous" and the membrane marker UAS-PLCδ-PH-mCherry "membrane". The top row depicts a medial section where the entire cell is visible. The bottom row is a zoomed-in view of the cleavage furrow. Time relative to start of imaging is indicated.

Video 4: Arp2/3 is required for plasma membrane oscillations and intercellular bridge constriction

Part 1: Arp2/3 complex and membrane dynamics during the late stages of NSC division. Super resolution videos of an NSC expressing Arp3-GFP "Arp 3" and the membrane marker UAS-PLCδ-PH-mCherry "membrane". The top row depicts a medial section where the entire cell is visible. The bottom row is a zoomed-in view of the cleavage furrow. Time relative to start of imaging is indicated. In post-processing, Guassian blur was applied to the GFP channel to reduce noise.

Part 2: SCAR/WAVE complex and membrane dynamics during the late stages of NSC division. Super resolution videos of an NSC expressing SCAR-GFP "SCAR" and the membrane marker UAS-PLCδ-PH-mCherry "membrane". The top row depicts a medial section where the entire cell is visible. The bottom row is a zoomed-in view of the cleavage furrow. Time relative to start of imaging is indicated. In post-processing, Guassian blur was applied to the GFP channel to reduce noise.

Part 3: The effects of Arp2/3 inhibition on membrane dynamics during the late stages of NSC division. Super resolution videos of NSCs expressing membrane marker UAS-PLCδ-PH-GFP "membrane" and treated with the Arp2/3 inhibitor CK666. The left column depicts a medial section where the entire cell is visible. The bottom row is a zoomed-in view of the cleavage

276 furrow. Time relative to start of imaging is indicated. Arp2/3 inhibition occurs early on during
277 cytokinesis in the first cell, whereas Arp2/3 becomes inhibited later in the second cell.

283 **Author Contributions**

284 B.L. and K.E.P. designed the experiments. B.L. performed the experiments. B.L. and K.E.P
285 analyzed the data, prepared the figures, and wrote the manuscript.
286
287 **Declaration of Interests**

288 The authors have no competing interests to declare.
289

290 **References**
291 1. Andrade, V., and Echard, A. (2022). Mechanics and regulation of cytokinetic abscission. Front. Cell
292 Dev. Biol. *10*, 1046617. https://doi.org/10.3389/fcell.2022.1046617.

293 2. Hu, C.-K., Coughlin, M., and Mitchison, T.J. (2012). Midbody assembly and its regulation during
294 cytokinesis. Mol. Biol. Cell *23*, 1024–1034. https://doi.org/10.1091/mbc.E11-08-0721.

295 3. Elia, N., Sougrat, R., Spurlin, T.A., Hurley, J.H., and Lippincott-Schwartz, J. (2011). Dynamics of
296 endosomal sorting complex required for transport (ESCRT) machinery during cytokinesis and its role
297 in abscission. Proc. Natl. Acad. Sci. U. S. A. *108*, 4846–4851.
298 https://doi.org/10.1073/pnas.1102714108.

299 4. Schiel, J.A., Simon, G.C., Zaharris, C., Weisz, J., Castle, D., Wu, C.C., and Prekeris, R. (2012). FIP3-
300 endosome-dependent formation of the secondary ingression mediates ESCRT-III recruitment during
301 cytokinesis. Nat. Cell Biol. *14*, 1068–1078. https://doi.org/10.1038/ncb2577.

302 5. Guizetti, J., Schermelleh, L., Mäntler, J., Maar, S., Poser, I., Leonhardt, H., Müller-Reichert, T., and
303 Gerlich, D.W. (2011). Cortical constriction during abscission involves helices of ESCRT-III-dependent
304 filaments. Science *331*, 1616–1620. https://doi.org/10.1126/science.1201847.

305 6. Burton, K., and Taylor, D.L. (1997). Traction forces of cytokinesis measured with optically modified
306 elastic substrata. Nature *385*, 450–454. https://doi.org/10.1038/385450a0.

307 7. Andrade, V., Bai, J., Gupta-Rossi, N., Jimenez, A.J., Delevoye, C., Lamaze, C., and Echard, A. (2022).
308 Caveolae promote successful abscission by controlling intercellular bridge tension during cytokinesis.
309 Sci. Adv. *8*, eabm5095. https://doi.org/10.1126/sciadv.abm5095.

310 8. Mierzwa, B., and Gerlich, D.W. (2014). Cytokinetic abscission: molecular mechanisms and temporal
311 control. Dev. Cell *31*, 525–538. https://doi.org/10.1016/j.devcel.2014.11.006.

312 9. Addi, C., Presle, A., Frémont, S., Cuvelier, F., Rocancourt, M., Milin, F., Schmutz, S., Chamot-Rooke,
313 J., Douché, T., Duchateau, M., et al. (2020). The Flemmingsome reveals an ESCRT-to-membrane

314   coupling via ALIX/syntenin/syndecan-4 required for completion of cytokinesis. Nat. Commun. *11*,
315   1941. https://doi.org/10.1038/s41467-020-15205-z.

316 10. Park, S., Dahn, R., Kurt, E., Presle, A., VanDenHeuvel, K., Moravec, C., Jambhekar, A., Olukoga, O.,
317   Shepherd, J., Echard, A., et al. (2023). The mammalian midbody and midbody remnant are assembly
318   sites for RNA and localized translation. Dev. Cell *58*, 1917-1932.e6.
319   https://doi.org/10.1016/j.devcel.2023.07.009.

320 11. Lata, S., Schoehn, G., Jain, A., Pires, R., Piehler, J., Gottlinger, H.G., and Weissenhorn, W. (2008).
321   Helical structures of ESCRT-III are disassembled by VPS4. Science *321*, 1354–1357.
322   https://doi.org/10.1126/science.1161070.

323 12. Bajorek, M., Schubert, H.L., McCullough, J., Langelier, C., Eckert, D.M., Stubblefield, W.-M.B., Uter,
324   N.T., Myszka, D.G., Hill, C.P., and Sundquist, W.I. (2009). Structural basis for ESCRT-III protein
325   autoinhibition. Nat. Struct. Mol. Biol. *16*, 754–762. https://doi.org/10.1038/nsmb.1621.

326 13. Lafaurie-Janvore, J., Maiuri, P., Wang, I., Pinot, M., Manneville, J.-B., Betz, T., Balland, M., and Piel,
327   M. (2013). ESCRT-III assembly and cytokinetic abscission are induced by tension release in the
328   intercellular bridge. Science *339*, 1625–1629. https://doi.org/10.1126/science.1233866.

329 14. Mollinari, C., Kleman, J.-P., Jiang, W., Schoehn, G., Hunter, T., and Margolis, R.L. (2002). PRC1 is a
330   microtubule binding and bundling protein essential to maintain the mitotic spindle midzone. J. Cell
331   Biol. *157*, 1175–1186. https://doi.org/10.1083/jcb.200111052.

332 15. Zhu, C., and Jiang, W. (2005). Cell cycle-dependent translocation of PRC1 on the spindle by Kif4 is
333   essential for midzone formation and cytokinesis. Proc. Natl. Acad. Sci. U. S. A. *102*, 343–348.
334   https://doi.org/10.1073/pnas.0408438102.

335 16. Mullins, J.M., and Biesele, J.J. (1977). Terminal phase of cytokinesis in D-98s cells. J. Cell Biol. *73*,
336   672–684. https://doi.org/10.1083/jcb.73.3.672.

337 17. Dionne, L.K., Wang, X.-J., and Prekeris, R. (2015). Midbody: from cellular junk to regulator of cell
338   polarity and cell fate. Curr. Opin. Cell Biol. *35*, 51–58. https://doi.org/10.1016/j.ceb.2015.04.010.

339 18. Penkert, R.R., LaFoya, B., Moholt-Siebert, L., Vargas, E., Welch, S.E., and Prehoda, K.E. (2024). The
340   Drosophila neuroblast polarity cycle at a glance. J. Cell Sci. *137*, jcs261789.
341   https://doi.org/10.1242/jcs.261789.

342 19. LaFoya, B., and Prehoda, K.E. (2023). Consumption of a polarized membrane reservoir drives
343   asymmetric membrane expansion during the unequal divisions of neural stem cells. Dev. Cell, S1534-
344   5807(23)00159-4. https://doi.org/10.1016/j.devcel.2023.04.006.

345 20. Homem, C.C.F., and Knoblich, J.A. (2012). Drosophila neuroblasts: a model for stem cell biology.
346   *139*, 4297–4310. https://doi.org/10.1242/dev.080515.

347 21. Cabernard, C. (2012). Cytokinesis in Drosophila melanogaster. Cytoskelet. Hoboken NJ *69*, 791–
348   809. https://doi.org/10.1002/cm.21060.

349 22. Roth, M., Roubinet, C., Iffländer, N., Ferrand, A., and Cabernard, C. (2015). Asymmetrically dividing
350   Drosophila neuroblasts utilize two spatially and temporally independent cytokinesis pathways. Nat.
351   Commun. *6*, 6551. https://doi.org/10.1038/ncomms7551.

352 23. Cabernard, C., Prehoda, K.E., and Doe, C.Q. (2010). A spindle-independent cleavage furrow
353   positioning pathway. Nature *467*, 91–94. https://doi.org/10.1038/nature09334.

354 24. Connell, M., Cabernard, C., Ricketson, D., Doe, C.Q., and Prehoda, K.E. (2011). Asymmetric cortical
355   extension shifts cleavage furrow position in Drosophila neuroblasts. Mol. Biol. Cell *22*, 4220–4226.
356   https://doi.org/10.1091/mbc.E11-02-0173.

357 25. Roubinet, C., Tsankova, A., Pham, T.T., Monnard, A., Caussinus, E., Affolter, M., and Cabernard, C.
358   (2017). Spatio-temporally separated cortical flows and spindle geometry establish physical
359   asymmetry in fly neural stem cells. Nat. Commun. *8*, 1383. https://doi.org/10.1038/s41467-017-
360   01391-w.

361 26. Pham, T.T., Monnard, A., Helenius, J., Lund, E., Lee, N., Müller, D.J., and Cabernard, C. (2019).
362   Spatiotemporally Controlled Myosin Relocalization and Internal Pressure Generate Sibling Cell Size
363   Asymmetry. iScience *13*, 9–19. https://doi.org/10.1016/j.isci.2019.02.002.

364 27. Montembault, E., Deduyer, I., Claverie, M.-C., Bouit, L., Tourasse, N.J., Dupuy, D., McCusker, D.,
365   and Royou, A. (2023). Two RhoGEF isoforms with distinct localisation control furrow position during
366   asymmetric cell division. Nat. Commun. *14*, 3209. https://doi.org/10.1038/s41467-023-38912-9.

367 28. Montembault, E., Claverie, M.-C., Bouit, L., Landmann, C., Jenkins, J., Tsankova, A., Cabernard, C.,
368   and Royou, A. (2017). Myosin efflux promotes cell elongation to coordinate chromosome segregation
369   with cell cleavage. Nat. Commun. *8*, 326. https://doi.org/10.1038/s41467-017-00337-6.

370 29. Vernì, F., Somma, M.P., Gunsalus, K.C., Bonaccorsi, S., Belloni, G., Goldberg, M.L., and Gatti, M.
371   (2004). Feo, the Drosophila homolog of PRC1, is required for central-spindle formation and
372   cytokinesis. Curr. Biol. CB *14*, 1569–1575. https://doi.org/10.1016/j.cub.2004.08.054.

373 30. Loyer, N., and Januschke, J. (2018). The last-born daughter cell contributes to division orientation of
374   Drosophila larval neuroblasts. Nat. Commun. *9*, 3745. https://doi.org/10.1038/s41467-018-06276-0.

375 31. Cazzagon, G., Roubinet, C., and Baum, B. (2023). Polarized SCAR and the Arp2/3 complex regulate
376   apical cortical remodeling in asymmetrically dividing neuroblasts. iScience *26*, 107129.
377   https://doi.org/10.1016/j.isci.2023.107129.

378 32. Sun, Y., Schöneberg, J., Chen, X., Jiang, T., Kaplan, C., Xu, K., Pollard, T.D., and Drubin, D.G.
379   (2019). Direct comparison of clathrin-mediated endocytosis in budding and fission yeast reveals
380   conserved and evolvable features. eLife *8*, e50749. https://doi.org/10.7554/eLife.50749.

381 33. Balzer, C.J., James, M.L., Narvaez-Ortiz, H.Y., Helgeson, L.A., Sirotkin, V., and Nolen, B.J. (2020).
382   Synergy between Wsp1 and Dip1 may initiate assembly of endocytic actin networks. eLife *9*, e60419.
383   https://doi.org/10.7554/eLife.60419.

384 34. Khuong, T.M., Habets, R.L.P., Kuenen, S., Witkowska, A., Kasprowicz, J., Swerts, J., Jahn, R., van
385   den Bogaart, G., and Verstreken, P. (2013). Synaptic PI(3,4,5)P3 Is Required for Syntaxin1A
386   Clustering and Neurotransmitter Release. Neuron *77*, 1097–1108.
387   https://doi.org/10.1016/j.neuron.2013.01.025.

388 35. Williams, A.M., Donoughe, S., Munro, E., and Horne-Badovinac, S. (2022). Fat2 polarizes the WAVE
389   complex in trans to align cell protrusions for collective migration. eLife *11*, 1–31.
390   https://doi.org/10.7554/eLife.78343.

391 36. Royou, A., Sullivan, W., and Karess, R. (2002). Cortical recruitment of nonmuscle myosin II in early
392   syncytial Drosophila embryos: Its role in nuclear axial expansion and its regulation by Cdc2 activity. J.
393   Cell Biol. *158*, 127–137. https://doi.org/10.1083/jcb.200203148.

394   37. Azuma, T., and Kei, T. (2015). Super-resolution spinning-disk confocal microscopy using optical
395   photon reassignment. Opt. Express *23*, 15003. https://doi.org/10.1364/oe.23.015003.
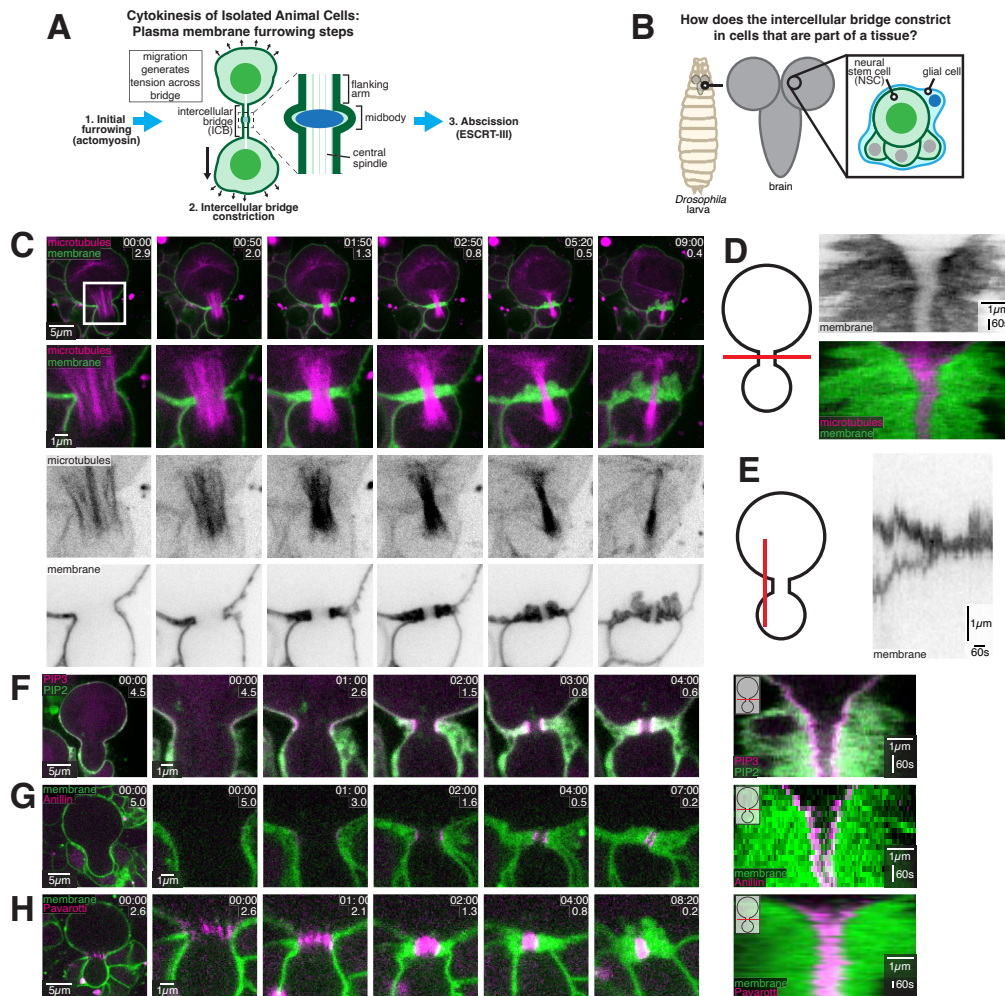
396

Figure 1   LaFoya and Prehoda

Figure 1: Larval brain neural stem cell intercellular bridges are midbodies without flanking arms

A) Intercellular bridge (ICB) constriction. Animal cell cytokinesis consists of three furrowing steps, the initial furrowing of the actomyosin ring, ICB constriction, and abscission. In isolated cells like cultured cells, the ICB is constricted by migration of the nascent siblings away from one another, which generates tension across the bridge. Constriction, or "thinning" of the ICB occurs at the flanking arms, leaving the central bulge from the midbody.

B) Larval brain neural stem cells (NSCs) are part of a complex tissue. *Drosophila* larval brain NSCs are surrounded by a cortex glial cell (blue) and progeny from previous divisions (smaller cells). This study uses the NSC as a model system for understanding how ICB constriction occurs in cells that are part of a tissue, where mechanical constraints may preclude the mechanisms used by isolated cells.

C) Membrane and microtubule dynamics during the late stages of NSC division. Selected frames from Video 1 are shown. Time in minutes relative to the start of imaging is shown, along with the diameter of the cytokinetic pore in microns.

D) Kymograph of membrane and microtubule dynamics across the cytokinetic furrow as the intercellular bridge forms and thins.

E) Kymograph demonstrating that during cytokinesis, nascent sibling cells are initially distanced from one another and then come in contact.

F) Phosphoinositide localization during the late stages of NSC division. Selected frames from Video 1 are shown. The NSC is expressing UAS-GRP1-GFP "PIP3" and UAS-PLCδ-PH-mCherry "PIP2". Time in minutes relative to the start of imaging is shown, along with the diameter of the cytokinetic pore in microns. To the right is a kymograph of phospho-inositide localization across the cytokinetic pore.

G) Anillin and membrane dynamics during the late stages of NSC division. Selected frames from Video 1 are shown. Time in minutes relative to the start of imaging is shown, along with the diameter of the cytokinetic pore in microns. To the right, a kymograph of Anillin and membrane dynamics across the cytokinetic pore is shown.

H) Pavarotti and membrane dynamics during the late stages of NSC division. Selected frames from Video 1 are shown. Time in minutes relative to the start of imaging is shown, along with the diameter of the cytokinetic pore in microns. To the right, a kymograph of Pavarotti and membrane dynamics across the cytokinetic pore is shown.
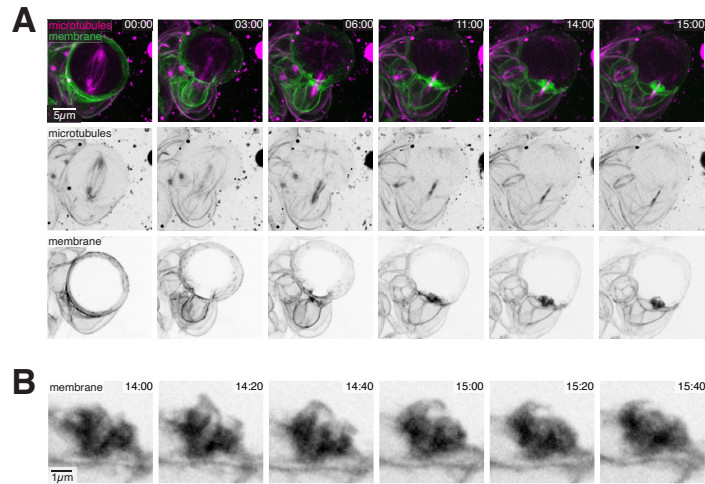
Figure 2
LaFoya and Prehoda

Figure 2: Plasma membrane oscillations near the cytokinetic pore during ICB formation and constriction

A) Membrane and microtubule dynamics during the late stages of NSC asymmetric division. Selected frames from Video 2 are shown. Maximum intensity projections of multiple optical sections spanning the cleavage furrow are shown. Time relative to anaphase onset is indicated.

B) An example membrane oscillation. The cytokinetic pore and surrounding membrane is shown over the course of a single membrane oscillation. Time relative to anaphase onset is indicated.
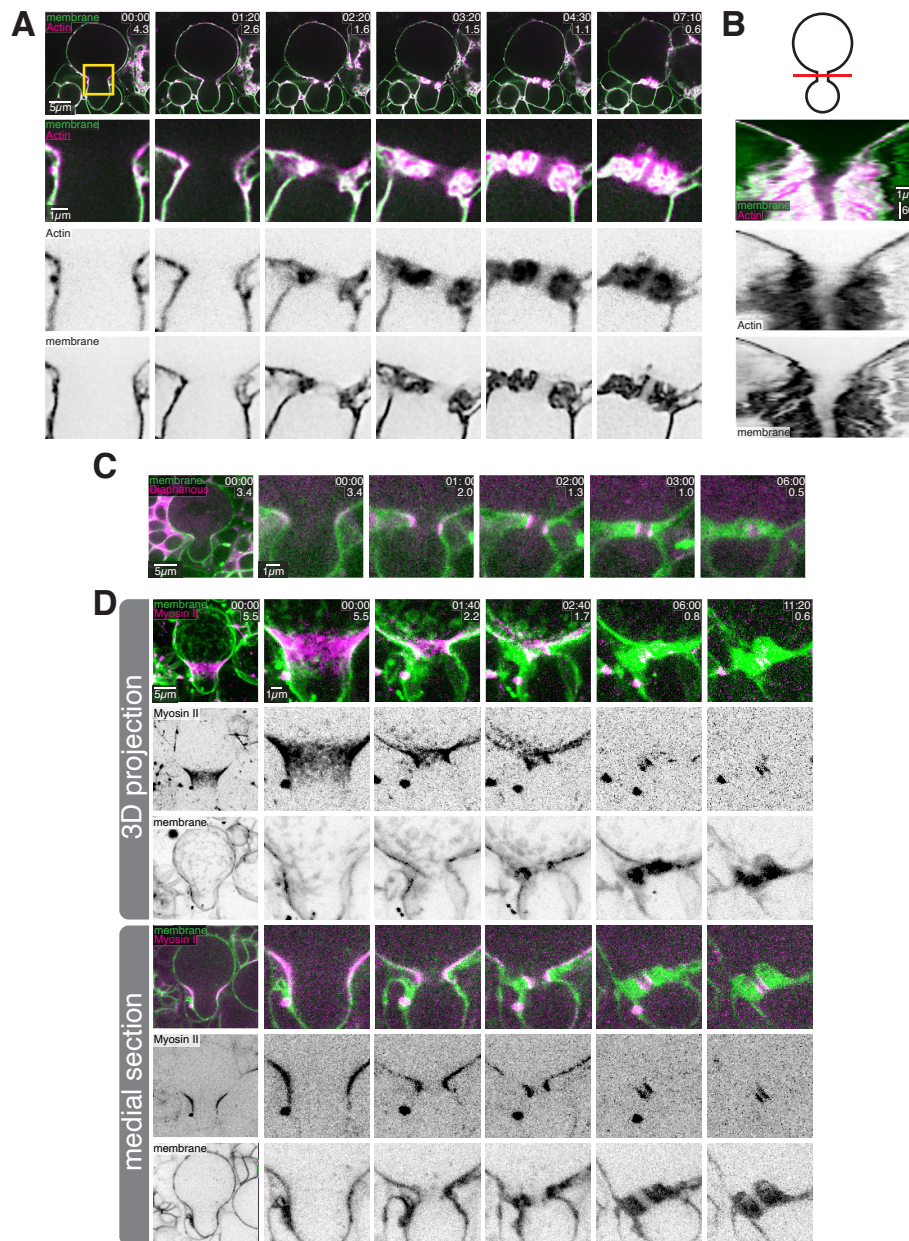
Figure 3   **LaFoya and Prehoda**

Figure 3: F-actin localizes to plasma membrane waves near the cytokinetic pore

A) F-actin and membrane dynamics during the late stages of NSC division. Selected frames from Video 3 are shown. The top row depicts a medial section where the entire cell is visible. The rows below are a zoomed-in view of the cleavage furrow. Time relative to the first frame is indicated, along with the diameter of the cytokinetic pore in microns. Image deconvolution was applied.

B) A kymograph of F-actin and membrane dynamics across the cytokinetic pore.

C) Diaphanous and membrane dynamics during the late stages of NSC asymmetric division. Selected frames are shown from Video 3. A medial section where the entire cell is visible (left) is next to a timelapse of a zoomed-in view of the cleavage furrow. Time relative to the first frame is indicated, along with the diameter of the cytokinetic pore in microns.

D) Myosin II and membrane dynamics during the late stages of NSC asymmetric division. Selected frames are shown from Video 3. The top 3 rows depicts maximum intensity projections of an entire hemisphere of the dividing NSC. The bottom row is a medial section. The left column shows a view of the whole cell, and the columns to the right are zoomed-in views of the cleavage furrow. Time relative to the first frame is indicated, along with the diameter of the cytokinetic pore in microns.
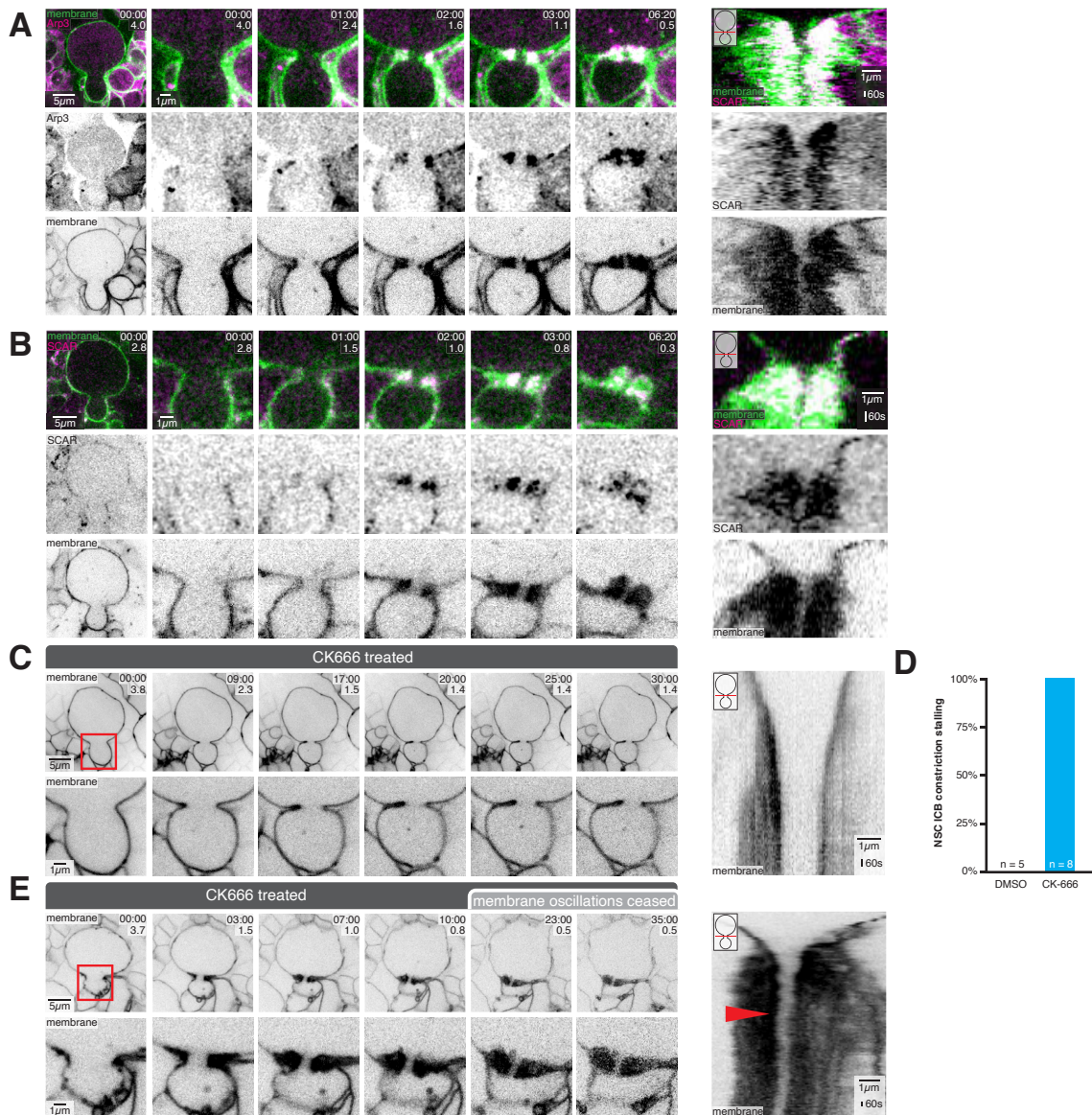
Figure 4   **LaFoya and Prehoda**

Figure 4: Arp2/3 is required for plasma membrane oscillations and ICB constriction

A) Arp2/3 complex and membrane dynamics during the late stages of NSC division. Selected frames from Video 4 are shown. A medial section where the entire cell is visible (left) is next to a timelapse of a zoomed-in view of the cleavage furrow. Time relative to the first frame is indicated, along with the diameter of the cytokinetic pore in microns. To the right is a kymograph of Arp2/3 complex and membrane dynamics across the cytokinetic pore.

B) SCAR complex and membrane dynamics during the late stages of NSC division. Selected frames from Video 4 are shown. A medial section where the entire cell is visible (left) is next to a timelapse of a zoomed-in view of the cleavage furrow. Time relative to the first frame is indicated, along with the diameter of the cytokinetic pore in microns. To the right is a kymograph of SCAR complex and membrane dynamics across the cytokinetic pore.

C) The effects of Arp2/3 inhibition on membrane dynamics during the late stages of NSC division. Selected frames from Video 4 are shown. The NSC was treated with the Arp2/3 inhibitor CK666 before the formation of the intercellular bridge (ICB). The left column depicts a medial section where the entire cell is visible. The bottom row is a zoomed-in view of the cleavage furrow. Time relative to start of imaging is indicated, along with the diameter of the cytokinetic pore in microns. To the right is a kymograph of membrane dynamics across the cytokinetic pore for the CK666-treated NSC.

D) Quantification of the effect of inhibition of Arp2/3 complex before ICB formation on late cytokinesis. NSCs from larval brains incubated with DMSO (carrier) or CK-666 before ICB formation were scored for stalled ICB constriction where the ICB did not reach a pore diameter of approximately 200 nm.

E) The same as in (C), except the NSC was treated with the Arp2/3 inhibitor CK666 after the formation of the intercellular bridge (ICB) and membrane oscillations had started. To the right is a kymograph of membrane dynamics across the cytokinetic pore for the CK666-treated NSC. The red arrow approximates when Arp2/3 was inhibited.